Inorganic Chemistry
Article
Cite This: Inorg. Chem. 2018, 57, 5463−5474
pubs.acs.org/IC

Exploring Lanthanide Doping in UiO-66: A Combined Experimental and Computational Study of the Electronic Structure

Kevin Hendrickx,[†,∥] Jonas J. Joos,[‡,§] Arthur De Vos,[∥] Dirk Poelman,[‡,§] Philippe F. Smet,[‡,§] Veronique Van Speybroeck,[*,∥] Pascal Van Der Voort,[*,†] and Kurt Lejaeghere[*,∥]

[†] Center for Ordered Materials, Organometallics and Catalysis (COMOC), Department of Inorganic and Physical Chemistry, Ghent University, Krijgslaan 281 (S3), 9000 Gent, Belgium

[‡] LumiLab, Department of Solid State Sciences, Ghent University, Krijgslaan 281 (S1), 9000 Gent, Belgium

[§] Center for Nano- and Biophotonics (NB Photonics), Ghent University, 9000 Gent, Belgium

[∥] Center for Molecular Modeling (CMM), Ghent University, Technologiepark 903, 9052 Zwijnaarde, Belgium

Supporting Information

ABSTRACT: Lanthanide-based metal−organic frameworks show very limited stabilities, which impedes their use in applications exploiting their extraordinary electronic properties, such as luminescence and photocatalysis. This study demonstrates a fast and easy microwave procedure to dope UiO-66, an exceptionally stable and tunable Zr-based metal−organic framework. The generally applicable synthesis methodology is used to incorporate different transition metal and lanthanide ions. Selected experiments on these newly synthesized materials allow us to construct an energy scheme of lanthanide energy levels with respect to the UiO-66 host. The model is confirmed via absolute intensity measurements and provides an intuitive way to understand charge transfer mechanisms in these doped UiO-66 materials. Density functional theory calculations on a subset of materials moreover improve our understanding of the electronic changes in doped UiO-66 and corroborate our empirical model.

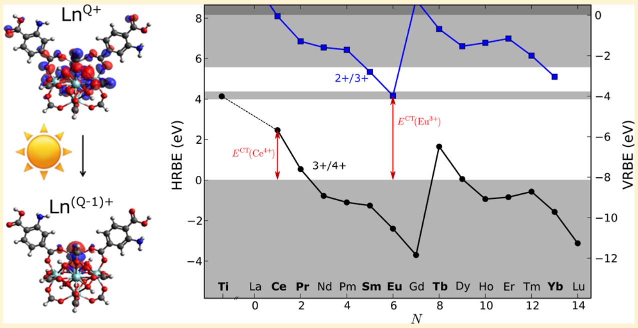

INTRODUCTION

Since their discovery, metal−organic frameworks (MOFs) have developed into a versatile platform for various applications, ranging from gas sorption and catalysis to sensing.[1−3] They owe this to their construction from inorganic clusters, linked together by organic bridges. This inherent modular nature makes it possible to design the materials at a molecular level and tune their properties for a specific application. Moreover, MOFs have recently emerged as photoactive materials, showing promising results in luminescence and photocatalytic applications.[4−8] One of the limiting factors in traditional semiconductor photocatalysts is the high electron−hole recombination rate. In MOFs, electrons are localized on distinct constituents. Hence, the organic linker may serve as the photoreceptive system (or antenna) and the inorganic node as the photocatalytically active center, which are separated entities within the same crystalline material. If the corresponding electronic bands are well-aligned, then an efficient separation and transfer between these sites can take place via a ligand-to-metal charge transfer (LMCT). Moreover, the modular setup of a MOF allows for an orthogonal engineering of the electronic structure, since linker and node contributions can be treated independently.[9]

In light-based applications, special attention goes to the series of lanthanide (Ln) metals. Their bright emission forms the basis of many lighting applications, and their specific electronic structure is ideally suited for catalytic fine chemistry.[10−12] Also within MOF research, Ln-based materials have emerged in recent years.[13−15] As Ln ions are inserted in a crystalline framework, they are heterogenized, facilitating the processing steps for several applications. Moreover, the orbital overlap between the antenna and the Ln ion can be ensured since they are part of the same rigid framework. The latter is of paramount importance to provide an efficient pathway for the charge carriers to move in the framework. Unfortunately, difficult syntheses and limited stability restrict the use of Ln MOFs.[16] To overcome this problem, we propose an approach inspired by solid-state lanthanide chemistry where a stable robust carrier material (e.g., a metal oxide) is doped with a small amount of lanthanide ions in a high-temperature process. Within this work, we adopt a microwave-based methodology to dope UiO-66, a robust MOF, with several lanthanide and transition metal ions and investigate the electronic properties of the new materials. So far, this doping strategy to alter the electronic properties was only used to introduce isovalent atoms.[17] However, thanks to the highly exchangeable nature of the constituents in MOF materials, we

Received: February 15, 2018
Published: April 16, 2018

ACS Publications

DOI: 10.1021/acs.inorgchem.8b00425
Inorg. Chem. 2018, 57, 5463−5474

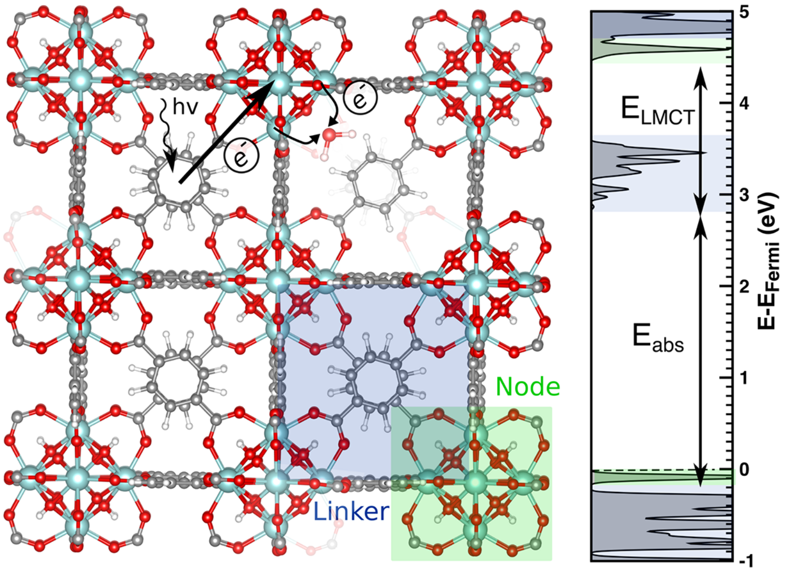

Figure 1. (left) Basic steps in a UiO-66 photocatalytic process: light absorption, LMCT and reduction process. (Right) Density of states of pristine UiO-66. Areas shaded in green indicate node contributions while areas shaded in blue indicate linker states.[9]

show that this methodology can be extended toward many more metals. The doping of a robust MOF with low concentrations of Ln dopant ions leads to a whole new series of materials which may advance a wide variety of applications, ranging from lighting to photocatalysis. Given the stability of the parent material, evaluation in different chemical environments and under different ambient conditions is possible while retaining the Ln-specific properties.

Challenges and Opportunities in Ln-Doping of UiO-66. UiO-66 is an often-used prototype MOF, also in light-based applications, due to its high tunability and unprecedented stability.[18] It is built out of 12-fold coordinated $Zr_6O_4(OH)_4$ inorganic bricks and benzene-1,4-dicarboxylate (BDC^{2-}) linkers.[19,20] The coordinative nature of the bonding in UiO-66 allows for an efficient postsynthetic exchange of both linkers and metals,[21] making UiO-66 the ideal platform for the exploration of new structures containing lanthanide dopant ions. Figure 1 represents the electronic structure of pristine UiO-66 and captures the basic idea of the LMCT process lying at the basis of the photocatalytic activity of the material. In an ideal situation, the aromatic BDC linker acts as an antenna to absorb light and generate an exciton. The excited electron should be able to move toward the inorganic node, reducing the zirconium from Zr^{4+} to Zr^{3+} which then becomes a redox active center.

UiO-66 in its pristine form is however poorly suited for photocatalysis. Besides its large band gap (4 eV), impeding excitation with light in the visible region of the spectrum, the major problem is the inefficient charge transfer between linker and node. Figure 1 shows that a transfer from the linker to the inorganic node will be very difficult, since the empty Zr d states lie more than 1 eV higher than the empty linker band (E_{LMCT}). This lack of overlap hinders the electron in traveling efficiently to the node.[9] In order to improve LMCT, changes to the LUCO states (lowest unoccupied crystalline orbital) are necessary. Introduction of Ti in the Zr node via postsynthetic exchange[22,23] was previously found to strongly improve the catalytic activity of the material due to a lowering of the d states.[24−30] Similarly, the 4f levels of Ln ions are expected to alter the HOCO−LUCO region of the material (HOCO: highest occupied crystal orbital).

Within this work we use for the first time a systematic experimental method to incorporate lanthanide ions in the UiO-66 framework and probe the electronic properties of these new materials. Although we provide insight into the electronic transitions (which result in their absorption/emission behavior) using demanding first-principles computational techniques, we also establish a more empirical model by exploiting recurrent features of the lanthanides. Indeed, systematic behavior emerges across the lanthanide series independent of the chemical environment, as all ions act chemically very similar. This behavior results in a typical zigzag curve for the charge state transition levels of lanthanide impurities in crystalline materials as a function of the used lanthanide. Thanks to the systematics, the location of the charge state transition levels for all lanthanides can be predicted when one knows the location of at least one such level for one lanthanide ion.[31−33] In this work, the systematic properties of the lanthanide ions are used to construct band diagrams of Ln-doped UiO-66, containing all 14 Ln (2+/3+) and (3+/4+) charge state transition levels, based on a small set of experimental absorption and photoluminescence (PL) spectra. To our knowledge, this is the first time a complex hybrid carrier material is evaluated using this methodology. Furthermore, a density functional theory (DFT) study of some of the selected materials corroborates the findings of the empirical model and helps to understand the electronic structure changes observed for the different doped frameworks. It bridges the gap between our novel Ln-MOFs and the existing isovalently doped materials.

■ EXPERIMENTAL AND COMPUTATIONAL DETAILS

Experimental Details. *Synthesis.* UiO-66 was synthesized based on a general procedure by Biswas and co-workers[34] (see Supporting Information section S1). The doping of the UiO-66 framework was performed using postsynthetic metal ion exchange inspired by a methodology developed by Lau et al. and Tu et al.[17] Materials were prepared doped with Ti^{4+}, Yb^{3+}, Eu^{3+}, Nd^{3+}, and Ce^{4+} and will be denoted as UiO-66:X^{n+}. To compare the spectroscopic properties of pure and doped UiO materials, a pure cerium-based UiO was also prepared. Synthesis of this UiO-66(Ce) was based on a procedure by Lammert et al.[35] Details of all syntheses are given in Supporting Information (section S1).

Structural Characterization. Ambient-temperature powder X-ray diffraction (PXRD) patterns were recorded on a Thermo Scientific ARL XTra diffractometer operating at 40 kV and 40 mA using Cu Kα radiation (λ = 1.5406 Å). The sorption isotherms were measured on a Belsorp Mini apparatus, operating at 77 K. Before the measurements, samples were dried for 4h at 80 °C in dynamic vacuum. All X-ray photoelectron spectroscopy (XPS) measurements were recorded on a S-Probe XPS spectrometer from Surface Science Instruments (VG) with monochromated Al (1486 eV) exciting radiation. Powder was positioned on the holder using conducting tape. In order to minimize charging, an electron flood gun of 3 eV was used as a neutralizer. All spectra were calibrated toward a C 1s peak position of adventitious carbon at 284.6 eV. For elemental mapping, a field-emission scanning electron microscope (FEI Quanta 200) operating at low vacuum was used, equipped with an energy dispersive X-ray spectrometer (EDX). Samples were measured with an electron beam accelerating voltage of 15 kV. Bright-field scanning transmission electron microscopy (BF-STEM) and EDX measurements were performed on a JEOL JEM-2200FS high-resolution STEM equipped with an EDX spectrometer with a spatial resolution of 0.13 nm, image lens spherical aberration corrector, electron energy loss spectrometer (filter), and field-emission gun (FEG) operating at 200 keV.

Spectroscopy. Solid-state ultraviolet/visible light (UV/vis) measurements were done on a Varian Cary 500 dual-beam UV/vis/NIR spectrophotometer using an internal 110 mm $BaSO_4$-coated integrating sphere. Liquid experiments were carried out in solvent (dimethylformamide) on a PerkinElmer Lambda 900 UV/vis/NIR spectrometer. For both emission and excitation photoluminescence spectra, a FS920 of Edinburgh Instruments was used. A high-pressure xenon arc lamp of 450 W was used as light source. The excitation wavelength was selected through a double excitation monochromator.

Empirical Model for Charge State Transition Levels. Lanthanide ions show similar properties irrespective of their chemical environment.[36] When incorporated as impurities in a given host material, a typical zigzag curve can be constructed for their charge state transition levels as a function of the 4f occupation number using the energies of the charge transfer bands observed in experimental spectra. This methodology is reviewed in refs 31−33 and is known to give transition level locations of lanthanide impurities in inorganic crystals within accuracies of a few 100 meV. Recently, an extension of the empirical rules was proposed toward titanium.[37]

Computational Details. In addition to the empirical model used to construct the Ln charge state transition levels, we also opted to further unravel the electronic properties of a carefully selected subset of samples by using DFT and time-dependent DFT (TDDFT). Because excited state calculations on periodic systems are still challenging within current computational models, we first performed TDDFT calculations on some well-defined clusters. These calculations allowed us to study the possible excitations and yielded qualitative information on the orbitals involved. Afterward periodic DFT calculations revealed the ground state band structures of the pristine UiO-66, UiO-66(Ti), UiO-66(Hf), and UiO-66(Ce) material. Since the behavior of Ln ions is notoriously difficult to predict with DFT, we only performed UiO-66(Ln) calculations with Ce^{4+}. Because Ce^{4+} contains no 4f or 5d electrons, the electron correlation is limited and DFT has been shown to provide reasonable qualitative results.[38,39]

Calculations on Cluster Models. Calculations on cluster models were performed in Gaussian09[40] using DFT and TDDFT on a series of simplified model systems. Both clusters with stoichiometry $Zr_{6-x}X_xO_4(OH)_4(HCOO)_{12}$ and $Zr_{6-x}X_xO_4(OH)_4(HCOO)_{10}(HBDC)_2$ were used to investigate the influence of the dopant ion. Previous research[41] has shown that the combination of the B3LYP[42,43] functional with a triple-ζ Def2TZVP basis set[44] is a good choice for these cluster calculations and hence we applied the same settings in this work. Geometry optimization of the clusters was performed on the same level.

Two types of calculations were performed. In order to mimic the cluster after excitation and LMCT of the framework, we performed ground-state DFT calculations on the model cluster with one extra electron.[45] In this way, the system is forced in a doublet spin state and a charge of −1. This allowed us to look into the ideal case where the electron efficiently transfers to the inorganic node, and to study the potential preferential sites in these nodes for the electron to reside. Actual modeling of excited states is computationally much more demanding. TDDFT within its linear-response formulation offers a way to calculate vertical transition energies, which can be linked to experimental UV/vis spectra.[46−48] To visually improve the similarity with the experimental spectra, a Gaussian distribution (σ = 0.4 eV) was used to broaden the theoretical transition energies.

Periodic Models. Periodic calculations were performed on a 4-node unit cell within the VASP package,[49,50] using the Projector Augmented Wave approach (PAW)[51] with the recommended high-precision VASP 5.4 GW PAW potentials[52] and the PBE functional.[53] The plane-wave basis set had a kinetic energy cutoff of 700 eV, and a Γ-only grid was used to sample the first Brillouin zone. The equilibrium volume was obtained using a Rose-Vinet equation-of-state fit (9 points between −4 and 4% of the equilibrium volume),[54] and the structures were relaxed at this volume. An ionic energy criterion of 10^{-4} eV was used for all relaxations, and an electronic convergence criterion of 10^{-5} eV or 10^{-7} eV was applied for the equation of state points and equilibrium structures, respectively. Densities of states (DOS) were calculated using a Γ-centered $2 \times 2 \times 2$ grid and a 10^{-7} eV electronic convergence threshold.

RESULTS AND DISCUSSION

The first part of this work provides an overview of our experimentally produced UiO-66 samples and describes their synthesis and structural characterization in detail. Second, spectroscopic techniques are used to probe the electronic structure of the samples. Using these experimental data, we then reconstruct the typical lanthanide "zigzag" curve of the (2+/3+) and (3+/4+) charge state transition levels relative to the UiO-66 band diagram. Finally, we use DFT calculations on cluster and periodic models to obtain more insight in the charge transfer processes in titanium- and lanthanide-doped materials.

Synthesis and Structural Characterization. We doped UiO-66 with 5 different lanthanide and transition metal ions using a postsynthetic cation exchange method (see Table 1). Postsynthetic cation exchange is a technique that allows the modification of existing stable materials and the production of systems with otherwise unreachable compositions.[21,22,55] It is only in the past decade that the cation techniques applied to other inorganic materials[56−58] came into use within MOF chemistry. We used a microwave-assisted approach inspired by

Table 1. Overview of Samples Studied in This Work[a]

sample name	metal ion concentrations	linker
UiO-66	100% Zr^{4+}	BDC
UiO-66(Ce)	100% Ce^{4+}	BDC
UiO-66(Ce)-fum	100% Ce^{4+}	Fum
UiO-66:Ce^{4+}	1−5% Ce^{4+}	BDC
UiO-66-NH_2:Ce^{4+}	1−5% Ce^{4+}	BDC-NH_2
UiO-66:Nd^{3+}	1−5% Nd^{3+}	BDC
UiO-66:Eu^{3+}	1−5% Eu^{3+}	BDC
UiO-66:Yb^{3+}	1−5% Yb^{3+}	BDC
UiO-66:Ti^{4+}	5% Ti^{4+}	BDC
UiO-66-NH_2:Ti^{4+}	5% Ti^{4+}	BDC-NH_2

[a] Doped samples are indicated as UiO-66:X^{n+}. Ion concentrations are obtained by fitting of the (TEM/SEM)-EDX results and are prone to large errors. However, similar loadings were obtained for all samples. The loading of the UiO-66:Ti^{4+} was verified via inductive coupled plasma optical emission spectroscopy (ICP-OES). BDC stands for benzene-1,4-dicarboyxlic acid, BDC-NH_2 is 2-amino-benzene-1,4-dicarboxylic acid and fum represents fumaric acid. Note that UiO-66-fum is more generally known as MOF-801.[59]

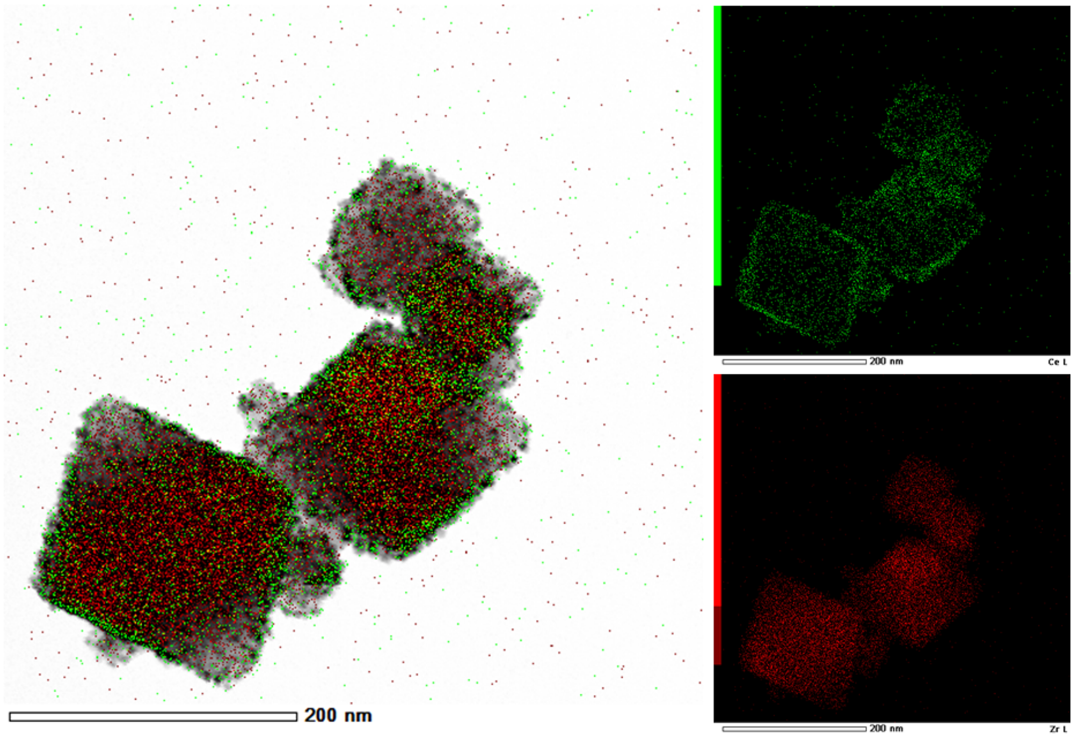

Figure 2. BF-STEM EDX profiles of Ce atoms (green) and Zr atoms (red) within a UiO-66:Ce^{4+} sample.

Tu et al.,[17] which compared to a conventional solvothermal approach allows for a drastic reduction in synthesis time from about a week to only a few hours to obtain a similar loading. We based our procedure on this doping strategy and extended its application to the incorporation of lanthanide ions as dopant in the framework.

A thorough experimental characterization was performed for all samples shown in Table 1, and the data are provided in Supporting Information (section S2). Our measurements show that after the cation exchange, all samples retained their crystallinity and porosity. Moreover, the shift of the low-angle diffraction peaks and the fact that no new peaks are observed in the XRD diffractogram seem to suggest that dopant ions are included on a Zr site and that no other Ti—O or Ln—O species are formed. However, whether dopant ions are inserted on a Zr position in the metal node or are adsorbed at a defect site is still subject to much debate.[60] Direct proof is very hard to obtain, and this matter remains open for discussion. Nitrogen sorption measurements (see Supporting Information) confirm that the UiO samples preserve a high surface area, but a partial blocking of the pores by adsorbed metal precursors cannot be a priori excluded. A combination of the two effects may also occur.

The distribution of the dopant ions was verified using BF-STEM EDX measurements. Figure 2 shows that the Ce^{4+} ions are distributed quite homogeneously and no cluster formation is observed. We however notice that some surface enrichment can be seen, probably due to diffusion limitations of the precursor in the material. Similar measurements were performed on Eu^{3+}- and Yb^{3+}-doped samples (see Figures S2 and S3). In the following sections, our focus will be mainly on the Ce^{4+}- and Eu^{3+}-doped materials. This gives sufficient information to construct the charge state transition zigzag curve for both (2+/3+) and (3+/4+) transitions. Results will be compared to either experiments or DFT calculations on pristine UiO-66 and Ti- or Hf-containing materials. For completeness spectra of all doped samples are provided in the Supporting Information.

Spectroscopy. UV/vis and photoluminescence (PL) measurements were performed to probe the electronic structure of the UiO materials. The former give information on direct transitions, directly related to the band gap of the material. Interpretation of the latter is more involved, since excited-state relaxations and intersystem conversions can occur before a photon is emitted by the material. Combination of the two techniques allows to understand the electronic structure of the materials on a fundamental level and provides the necessary information for the construction of the Ln zigzag curve.

UV/Vis Measurements of Doped UiO-66:X^{n+}. When assessing the electronic properties of photoactive doped UiO materials, it is instructive to compare the new materials to the known titanium-doped UiO-66. Figure 3 shows the UV/vis Kubelka—Munk function obtained from diffuse reflectance measurements for pristine UiO-66 and UiO-66:Ti^{4+} and for their amino-functionalized counterparts. As was previously established, the amine group of the linker-functionalized material has a large effect on the absorption edge (region **B** in Figure 3).[41] In comparison, the introduction of Ti leads to a shift and broadening of the UV edge due to the strong Ti—O—Zr interactions (region **A** in Figure 3). The interaction of the metal node with the linker also leads to a shift of the NH_2 absorption for the amine-functionalized materials (region **C** in Figure 3). The influence of the nearby metal node on the absorption maximum of the linker (regions **A** and **C**) has been observed in literature[24,26] and will be discussed in more detail later in the "Computational Assessment" section of this work.

Figure 4 shows the UV/vis spectra of UiO-66:Ce^{4+} and UiO-66-X(Ce) (X = BDC and fumaric acid (fum)) compared to pristine UiO-66 and UiO-66-NH_2. UV/vis spectra of the other lanthanide-doped materials are provided in the Supporting Information. We find that independent of the chosen linker

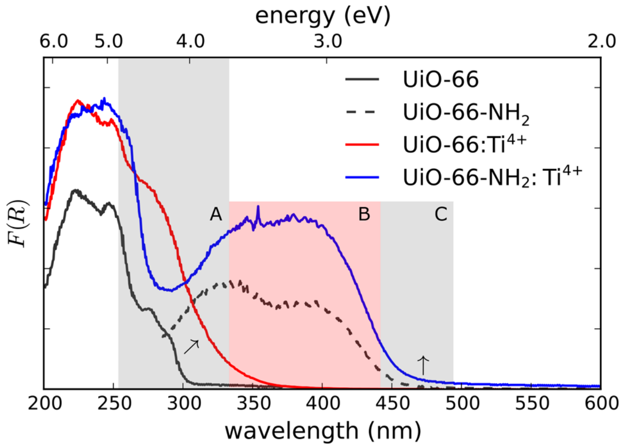

Figure 3. UV/vis spectra in Kubelka−Munk units of pristine UiO-66 and UiO-66-NH$_2$ materials compared to Ti-doped frameworks. Band **A** shows how the excitation of the aromatic system is influenced by the metal node. The black arrow indicates the shift caused by the changing environment of the linker. Band **B** corresponds to the absorption of the NH$_2$ group. Band **C** shows the change in the NH$_2$ absorption due to the interaction with Ti. Here again, the arrow indicates the shift caused by titanium.

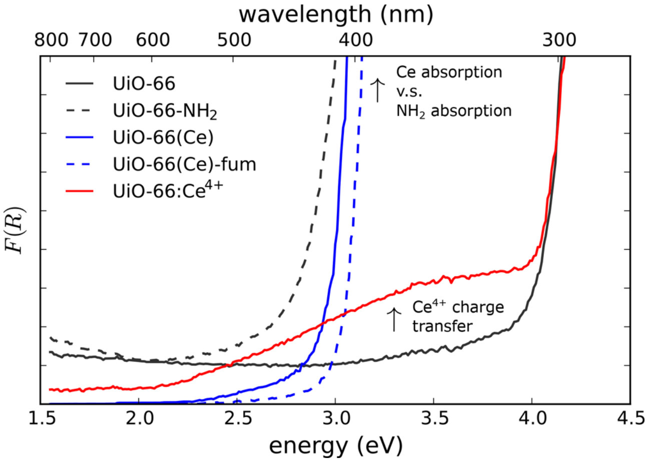

Figure 4. UV/vis spectra in Kubelka−Munk units of a series of different Ce^{4+} UiO samples compared to pristine UiO-66 and UiO-66-NH$_2$. For the nomenclature, see Table 1.

(fumaric acid or BDC), the absorption edge of UiO-66-X(Ce) is the same. This indicates that the main absorption in this material is due to a node-based transition rather than a linker transition like in pristine UiO-66. Moreover, the change in band gap is coincidentally about the same as induced by addition of a NH$_2$ functional group to the linker. We will show in the "Computational Assessment" section that this is because insertion of cerium in the inorganic node introduces a new band within the band gap of the pristine UiO-66, similar to what happens in amino-functionalized UiO-66.

Contrary to the pure cerium materials, the doped UiO-66:Ce^{4+} shows an edge at 4 eV. This transition is similar to the one in pristine UiO and corresponds to the BDC linker. However, a new broad band arises in the spectrum, starting at 2.5 eV, which we attribute to a charge transfer process. This band is most likely due to the O^{2-}−Ce^{4+} LMCT process, and we will refer to the corresponding energy as E_{CT} to avoid confusion with E_{LMCT} as defined in Figure 1 ($E_{CT} = E_{gap} + E_{LMCT}$ with $E_{LMCT} < 0$ for UiO-66:Ce^{4+}). The position of this band will be used to construct the charge state transition level curve for the (3+/4+) transition further on.

Photoluminescence Measurements. Eu^{3+} represents one of the spectroscopically most investigated lanthanide ions due to its characteristic red luminescence lines.[61] A typical Jablonski diagram of a generic Eu^{3+}-doped material is presented in Figure 5 and shows the different pathways that can occur after absorption of a photon by the material. The excited linker can quickly decay to its ground state (fluorescence) or the electron can be transferred via an intersystem crossing to a triplet state and then to the Eu^{3+} impurity. From there it decays to different low-lying Eu^{3+} levels, giving rise to characteristic peaks in the emission spectrum.

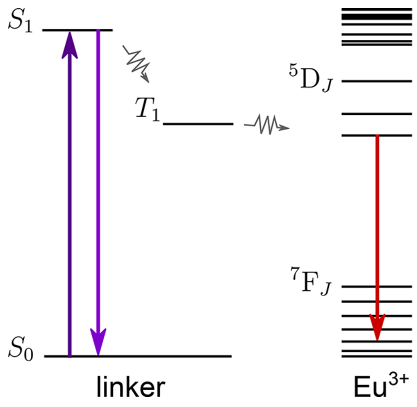

Figure 5. Simplified Jablonski diagram showing the energy transfer processes in a generic Eu^{3+}-doped material. Solid lines indicate the absorption or emission of a photon and curved lines are nonradiative transitions.

Figure 6 shows the emission and excitation spectra of the UiO-66:Eu^{3+} sample. The red line shows a broad linker emission band ranging to about 550 nm (see Supporting Information section S3) followed by the characteristic Eu^{3+} intraconfigurational 4f^6 lines.[61,62] By measuring the excitation spectrum for emission at wavelengths in these two different regions, we can investigate the mechanisms leading to this specific emission. At 460 nm, only linker emission is found and no Eu^{3+} emission. The excitation spectrum for emission at this wavelength hence shows the characteristic broad band absorption which is also observed for pristine UiO-66 (Supporting Information section S3) and which corresponds to photon absorption of the linker followed by

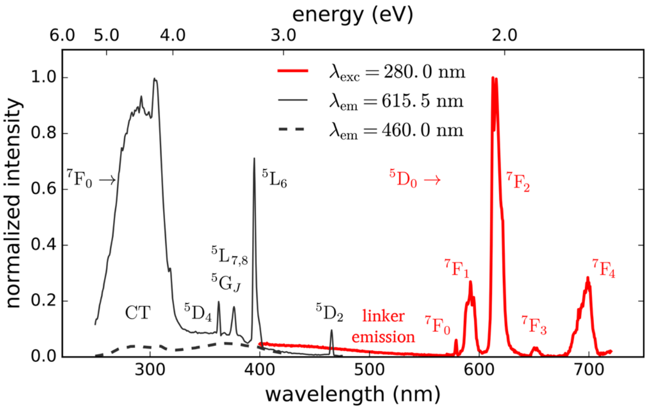

Figure 6. Emission and excitation spectrum of UiO-66:Eu^{3+} measured at 230 K.

fluorescent decay. If we however look at the spectrum measured at an emission of 615.5 nm, corresponding to the $^5D_0 \rightarrow {}^7F_2$ transition of Eu^{3+}, then more features arise. The narrow lines correspond to direct excitation channels of the Eu atoms with following fluorescent decay. In addition, we observe a broad band which we associate with a charge transfer band. We attribute this excitation to the O^{2-}−Eu^{3+} CT and the value of the edge (300 nm, 4.1 eV) will be used to position the (2+/3+) transition levels of all other lanthanides in the next section.

Charge State Transition Levels. The limited sensitivity of lanthanides to the chemical environment leads to a systematic behavior of various physical properties across the lanthanide series, resulting in a typical zigzag curve. Such curves are often constructed in Ln-doped oxides to predict the charge state transition energies of the whole series by means of only a few experimental data points. These levels are usually compared to the band edges of the host electronic structure (host-referred binding energy, HRBE). The CT offset obtained from the UV/vis data positions the Ce(3+/4+) level at 2.5 eV with respect to the HOCO. The position of this data point fixes the relative energies of the other lanthanides (black line in Figure 7).

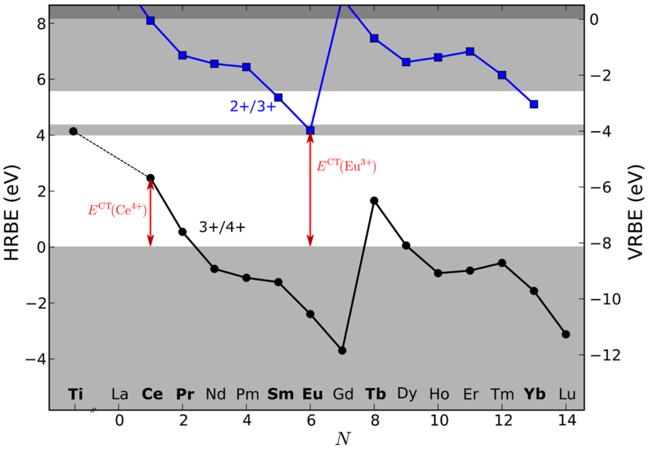

Figure 7. Overlay of the band diagram of UiO-66 (gray) with both the (3+/4+) (black dots) and (2+/3+) charge state transition levels (blue squares) for the lanthanide series incorporated as impurities in the UiO-66 host. Elements with a potentially interesting transition level for photocatalysis are printed in bold. The curves are calibrated using the CT absorption edges obtained for UiO-66:Ce^{4+} (3+/4+) and UiO-66:Eu^{3+} (2+/3+) as indicated by the red arrows. Titanium can also be included using a recently proposed expansion of the empirical model.[37] Values are referred to the vacuum (VRBE, vacuum-referred binding energy) or relative to the host material (HRBE, host-referred binding energy).

Positioning of the (2+/3+) transition curve was possible from the PL measurements performed on UiO-66:Eu^{3+}. The associated CT was found to occur at 4.1 eV, which fixes the Eu(2+/3+) charge state transition energy and as a result the complete (2+/3+) curve (blue line in Figure 7). Rogers et al. moreover found that the $Ti^{(3+/4+)}$ transition level can be found at approximately the same binding energy value as the $Eu^{(2+/3+)}$ transition level.[37] Because of the relevance of Ti-doped UiO-66, this transition level was also added to Figure 7.

Note that the Coulomb correlation energy U, defined as the difference between two successive charge state transition levels, amounts to 6.87 eV for Eu. This is a typical value for Eu in oxides (e.g., Dorenbos et al.[63]), which confirms our correct interpretation of the excitation/emission spectra. We can moreover use U to determine the vacuum level in the band diagram via the chemical shift of Eu^{2+}.[31] It allows the expression of all binding energies relative to this value (vacuum-referred binding energy, VRBE).

From the diagram in Figure 7, it is observed that the $Ti^{(3+/4+)}$ level and hence the CT of Ti^{4+} is resonant with the material's HOCO−LUCO gap, explaining the improved electron mobility of UiO-66:Ti^{4+} after excitation. The overlap between the $Ti^{(3+/4+)}$ level and the LUCO of UiO-66 is believed to be the cause for the increased photocatalytic activity for UiO-66:Ti^{4+}, since an excited electron of the linker has sufficient energy to move to the dopant ion. Following the same reasoning, all Ln ions with (3+/4+) or (2+/3+) charge state transition levels near or below the UiO-66 LUCO region could potentially be the target of an LMCT process upon excitation of the UiO host (e.g., Pr, Sm, or Tb). In order to validate this assumption, the transfer is investigated in the next section via absolute luminescence intensity measurements. Furthermore, DFT calculations will be performed on Ti- and Ce-doped samples to corroborate our findings.

Absolute Intensities. From the PL measurements, we know that the unfunctionalized linker shows a broad band emission centered around 400 nm (see Supporting Information section S3). This band is due to the recombination of the exciton, centered on the linker, with emission of a photon. The doped UiO materials aim to impede this direct recombination pathway by inducing energy transfer to the metal ions. The opening of the new decay channel competes with the direct recombination, resulting in a decrease of the linker emission band. The more efficient the LMCT process, the stronger the reduction of the linker emission, offering a method to assess the efficiency of the energy transfer via LMCT.

The most simple semiquantitative method to compare absolute emission intensities of powder samples consists of measuring an "infinitely" thick sample. This is done by using a filled cup that is placed in the standard PL setup. Since the incident light beam illuminates the entire sample, the emission can be compared among different samples in the same setup.

Table 2 shows the integrated intensities of the linker emission band of the different doped UiO samples. They are normalized to the pure UiO-66 emission and are based on the emission spectra provided in Supporting Information (section S3). One can observe that by doping the material, the resulting linker emission diminishes, suggesting that it is now in competition with alternative pathways. We see that Ti^{4+}, Eu^{3+}, Yb^{3+}, and Ce^{4+} all lead to a drastic decrease in intensity. For Ti and Eu, we already discussed their beneficial influence on the charge transfer pathway in UiO-66. Indeed, Table 2 corroborates that an efficient LMCT can take place and the emission intensity drops substantially. For the Ce^{4+} sample, almost a complete loss of the

Table 2. Integrated Intensities of the Linker Emission Band between 350 and 500 nm Excited at 300 nm[a]

sample	integrated intensity (%)
UiO-66	100
UiO-66:Ce^{4+}	6
UiO-66:Nd^{3+}	71
UiO-66:Eu^{3+}	12
UiO-66:Yb^{3+}	14
UiO-66:Ti^{4+}	31

[a] The results are normalized to the UiO-66 emission.

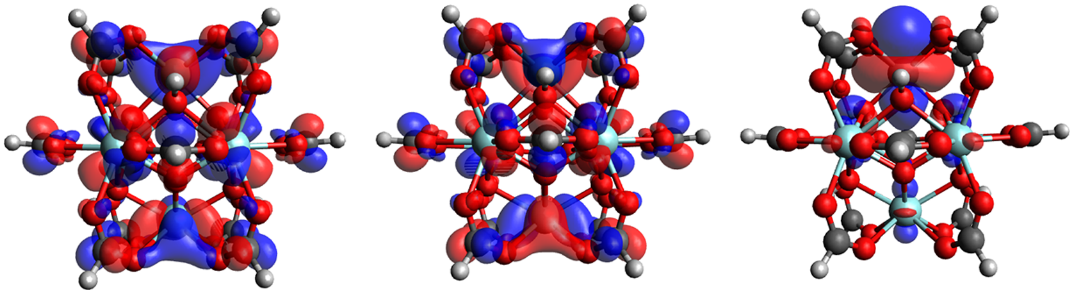

Figure 8. Cluster models of $Zr_6O_4(OH)_4(HCOO)_{12}$ (left), $Zr_5Hf_1O_4(OH)_4(HCOO)_{12}$ (middle, Hf is the top metal atom), and $Zr_5Ti_1O_4(OH)_4(HCOO)_{12}$ (right, Ti is the top metal atom) calculated at the B3LYP/DEF2TZVP level with a −1 charge and doublet spin state. The models show the localization of the additional electron on the titanium 3d shell (right).

emission peak is found. This could also be attributed to a fast energy transfer but possibly followed by fast energy dissipation via nonradiative pathways, for which Ce^{4+} is notorious.[64,65]

We also have a look at the other lanthanides not thoroughly discussed in the previous sections. About the same drop in intensity as for Eu^{3+} and Ce^{4+} can be found for Yb^{3+}. Figure 7 shows that the interband transition of the host material resonates with the (2+/3+) charge state transition level of the Yb ion, opening a decay pathway via this channel and hence lowering the linker-based emission peak. However, incorporation of Nd^{3+} leads to a much smaller decrease in intensity. This behavior is because the $Nd^{(2+/3+)}$ charge state transition occurs at a too high energy with respect to the LUCO (Figure 7), implying that a Nd charge transition will likely not occur.

Figure 7 shows that many more possibilities arise for an efficient LMCT, since Sm and Tb also show charge state transition levels within the UiO-66 band gap. Further investigation of the different Ln-doped UiO-66 materials can yield more insight in the decay pathways and could lead to materials with improved luminescent properties or increased photocatalytic activity. However, as the results show, the resonance of the Eu or Yb charge state transitions with the HOCO-LUCO energy gap indicates that these doped materials would be first of choice for a further study.

Computational Assessment. In order to gain more insight at a fundamental level, a selected subset of the samples was assessed from first principles. Excited-state calculations are still challenging for periodic systems, so we performed TDDFT calculations on some well-defined clusters. We focused on isovalent dopant ions (Ti or Hf), which do not offer computational difficulties and may serve as a reference. In addition, ground state calculations were used to simulate isovalently substituted UiO-66 with a single negative charge (and doublet spin state). This model represents the cluster after charge transfer from the linker. Observation of the singly occupied molecular orbital (SOMO) then yields insight in the localization of this excess negative charge. Periodic data are presented afterward and offer insights in the ground state electronic structure, which can be qualitatively linked to the observed changes in the experimental data.

Cluster Models. First, we performed calculations on a series of simplified cluster models, consisting of one inorganic node terminated with formic acid. These clusters result in a total stoichiometry of $Zr_{6-n}M_nO_4(OH)_4(HCOO)_6$ (M = Ti^{4+} or Hf^{4+}). Three particular geometries are shown in Figure 8. The SOMO of both the pristine Zr node (left) and a Hf-doped one (middle) indicate that an extra electron is uniformly distributed over the whole node. If we however insert a titanium atom (right), then the electron is localized on the empty 3d orbitals of the Ti atom.

Even though these small clusters do not contain any aromatic linkers, and are therefore severely simplified model systems, inspection of the TDDFT spectra shows some interesting results (Figure 9). The Hf-doped node shows an almost identical spectrum as the pristine Zr node. In contrast, a peak arises around 320 nm caused by the inserted Ti. As the number of Ti atoms in the cluster increases, both the oscillator strength of this transition and the absorption in the spectrum rise. Closer investigation learns that it concerns a transition from oxygen-centered p-orbitals (oxygen from the formate anions) toward the Ti 3d orbitals. It can be linked to the shift observed experimentally in the A region of Figure 3. Moreover, the predicted position of this CT band agrees well with both experimental (Figure 3) and empirical results (Figure 7). As a final remark, it should be noted that the 100% titanium UiO has not yet been synthesized as such and has to be considered as a limiting case.

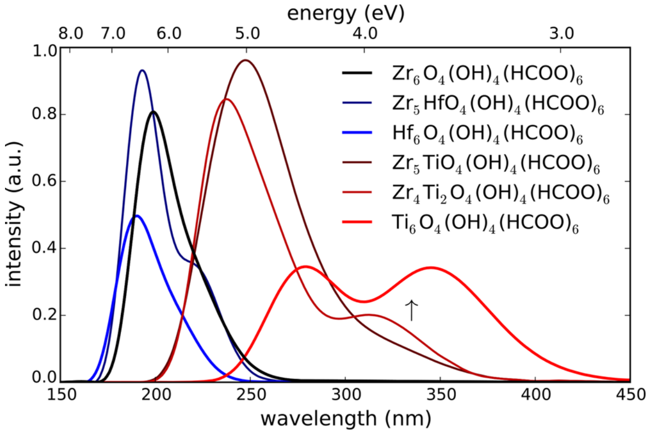

Figure 9. TDDFT spectra for simple formic acid terminated clusters with 1 or more Zr replaced by Hf of Ti. The arrow indicates the new peak rising as a function of the number of Ti atoms in the cluster and corresponds to an O^{2-}-Ti^{4+} excitation.

The simple cluster models allow to identify the absorption pathways that arise upon doping the UiO material. However, the artificial replacement of the linkers by formate anions results in a loss of linker states and is thus a severe approximation. We therefore studied more complex Ti-containing clusters, in which two formate capping molecules were replaced by BDC linkers, terminated by a hydrogen to secure charge balance. Since much interest has gone to the amine-functionalized variants, showing an even larger increase in photocatalytic activity, we also include an amine-modified cluster model in our calculations. The general cluster structure is shown in Figure 10 (inset), where atom X indicates the dopant and the *R*-group can be H or NH_2. The resulting spectra are shown in Figure 10.

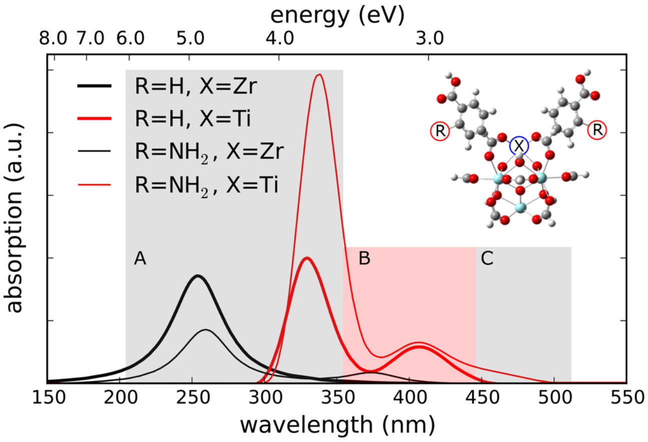

Figure 10. TDDFT absorption spectra (B3LYP/6-311+G(d,p), 30 states) for extended cluster models. The basic cluster model has a stoichiometry of $Zr_5XO_4(OH)_4$ $(HCOO)_{10}(BDC\text{-}R)_2$ with R = H and NH_2 and X = Zr and Ti (inset). The meaning of shaded regions **A**, **B**, and **C** is described in the text.

We notice that the results are qualitatively similar to those of Figure 9. A more detailed view on the three main features in the spectrum can be obtained by considering the related orbital transitions (see Figure 11). Region **A** of Figure 10 corresponds to the classical HOMO−LUMO excitation of the linker. The shift of this peak upon inclusion of a titanium atom agrees with the shift of absorption edges observed experimentally (indicated as region A in Figure 3). In region **B**, the BDC-NH_2 absorption arises as a small peak just below 400 nm, and there is a clear absorption caused by the included Ti. In this transition the most important contribution to the orbitals is moved from the p-orbitals of the oxygen atoms of the surrounding carboxylate groups to the Ti 3d orbitals (Figure 11B). This transition is similar to the one observed in the small cluster models shown in Figure 9. Finally, region **C** in Figure 10 contains a feature only observed in the amino-functionalized material. It shows a transition between the aromatic ring of the linker, more specifically the HOMO of the complete cluster, and a Ti 3d orbital. This transition only occurs when both an amine group and a Ti atom are present in the system. The existence of such a long-range charge transfer gives an indication as to why amine-functionalized UiO-66:Ti^{4+} shows the largest photocatalytic activity in literature.[24,25] These TDDFT findings therefore corroborate DFT calculations by Santaclara et al. for the situation where a Ti ion was grafted to a linker vacancy.[60]

Periodic Models. Further insight can be obtained by using a periodic model. We performed periodic DFT calculations of isovalently substituted UiO-66 and UiO-66(Ce). Figure 12 shows the DOS for the four considered structures, consisting of pure Zr, Hf, Ti, or Ce nodes. Pure UiO-66(Ti) has again to be considered as a theoretical limit. Note that although PBE is known to underestimate band gaps, it has been observed to reproduce trends correctly for UiO-66-type materials.[41] This is further confirmed by single-point HSE06 calculations[66,67] for UiO-66(Ti) and UiO-66(Ce) (see Supporting Information).

As shown by Figure 12, the DOS of the Zr and Hf material show almost no difference, since the electronic characteristics of the bare ions are very similar. This behavior was also found

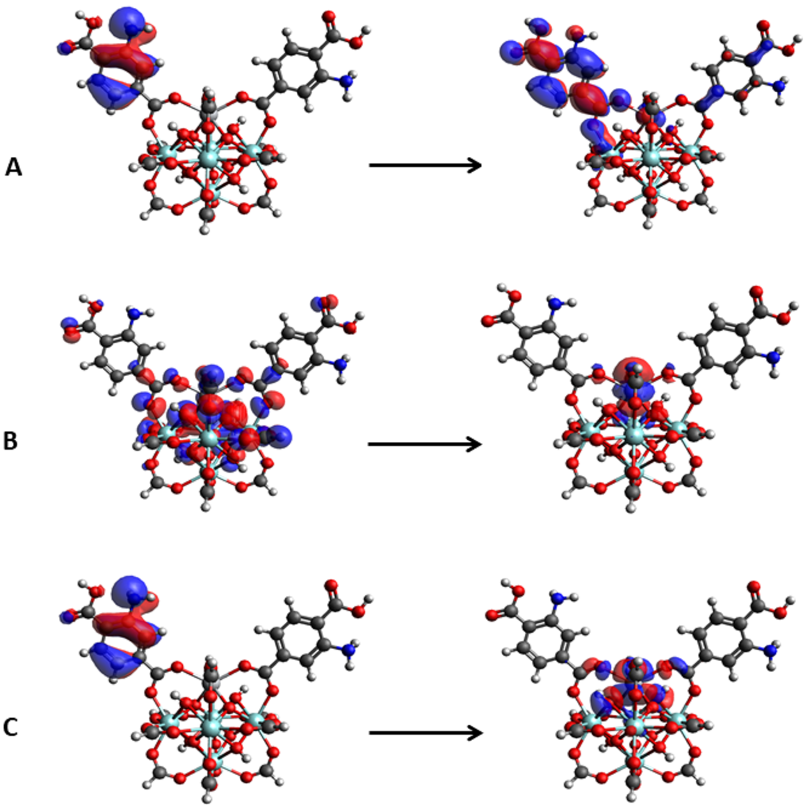

Figure 11. Orbitals contributing to the three main excitations observed in the spectrum of $Zr_5TiO_4(OH)_4(HCOO)_{10}(BDC\text{-}NH_2)_2$ (see Figure 10).

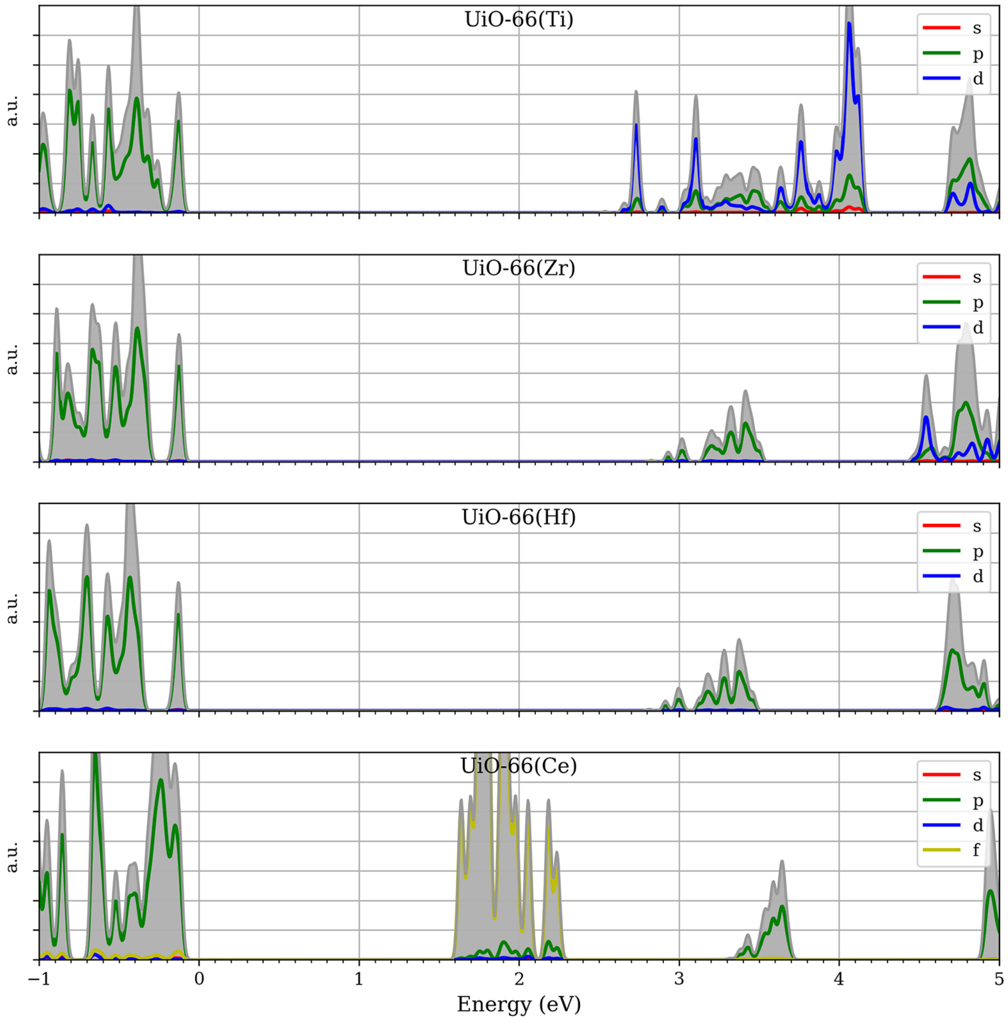

Figure 12. Total (gray) and projected (red, green, blue and yellow) density of states of (from top to bottom) UiO-66(Ti), UiO-66(Zr), UiO-66(Hf) and UiO-66(Ce). The energy is expressed with respect to the Fermi energy ($E_F = 0$).

experimentally by Nasalevich and co-workers[27] and using cluster calculations in the previous section. However, introducing titanium in the metal node alters the LUCO states of UiO-66. It introduces 3d states that are sufficiently low in energy to go below the linker-based band forming the LUCO of the pristine UiO-66. The overlap between the Ti 3d and the linker orbitals suggests better charge transfer possibilities and explains why an increased photocatalytic activity is observed for Ti-containing UiO-66. Note that Santaclara et al. reported that adsorbing Ti onto a linker vacancy would improve the activity even further.[60] Periodic calculations on UiO-66(Ce) show the appearance of a broad band within the original UiO HOCO-LUCO gap. This band consists of the 4f orbitals of the Ce ions. In the Ce^{4+} state, these orbitals are completely empty and hence form the new LUCO of the material. The LUCO therefore changes from ligand- to metal-based, similar to Ti-doped UiO-66, although no energetic overlap between the new and original LUCO states is now observed. Coincidentally, the Ce gap state appears at a similar energy from the HOCO as the state introduced by an amine group in UiO-66-NH_2 from the LUCO.[41] However, although the effect on the overall band gap is comparable (see Figure 4), both excitations are physically different. The amine group gives rise to a completely filled band and therefore creates a new HOCO state. This results in linker-based absorption. In contrast, cerium brings down the LUCO state and excitation occurs to a cerium level.

The observed Ce f band can be qualitatively linked to our previously obtained results. The occurrence of 4f levels in the band gap of UiO-66 indicates that Ce can take different charge states depending on the Fermi level location and that a charge transfer transition, measurable by optical spectroscopy, is to be expected. Indeed, the empty 4f band within the band gap of the pristine UiO-66 is energetically reachable for an electron that has been excited to the linker LUCO via an energy transfer process. The broad band observed in the absorption spectrum of Figure 4 was already attributed to this charge transfer channel. A charge state transition level must therefore be present in the band gap. The predicted location of the 4f band shows a good correspondence with the thermodynamic (3+/4+) charge state transition level, which was also used to construct Figure 7. The location of the Kohn−Sham single-particle levels (Figure 12) is not exactly the same as the location of the charge state transition level. This is however not to be expected given their different physical meaning.[68−71]

■ CONCLUSION

Lanthanide MOFs represent an interesting class of materials with specific electronic properties exploitable for luminescent and photocatalytic applications. Unfortunately, pure Ln-MOFs are notoriously unstable and difficult to synthesize. In this work, a simple microwave-assisted synthesis methodology was proposed for the fast incorporation of transition metal and lanthanide cations in the robust UiO-66 material, giving rise to an entire new set of highly stable materials with unprecedented electronic properties. Combining spectroscopic data with computational results allowed to understand the changes in electronic structure of the different materials in a synergistic way.

By using experimentally observed CT values in Ce- and Eu-doped UiO samples, the (2+/3+) and (3+/4+) charge state transition levels were predicted for the entire Ln series, displaying a zigzag curve with respect to the band structure of the host material (see Figure 7). Absolute intensity measurements confirmed this model, showing that for dopants with transition levels resonant to the HOCO−LUCO gap of UiO-66 an extra decay pathway becomes available. Further confirmation was obtained using DFT calculations. For isovalently substituted samples, only Ti shows a CT pathway. This is because Ti 3d levels overlap energetically with the linker LUMO state while Hf and Zr states only occur in a higher energy range. For Ln-doped materials, cerium insertion in the node introduces an empty 4f band within the pristine UiO-66 band gap, which also gives rise to CT. Similar charge transitions were observed for Yb and Eu. We therefore propose these Ln-based materials as prime candidates in catalytic studies. Moreover, the general applicability of our synthesis procedure combined with the stability of the proposed materials may encourage researchers to conduct further studies and open up a new chapter in Ln-MOF luminescence and photocatalytic studies.

■ ASSOCIATED CONTENT

Ⓢ Supporting Information

The Supporting Information is available free of charge on the ACS Publications website at DOI: 10.1021/acs.inorgchem.8b00425.

> Synthesis procedures; XRD diffractograms; BF-STEM EDX measurements; XPS scan of UiO-66:Ti^{4+}; nitrogen sorption isotherms; photoluminescence and UV/vis reflectance spectra; single-point HSE06 densities of states (PDF)

■ AUTHOR INFORMATION

Corresponding Authors

*E-mail: Veronique.VanSpeybroeck@UGent.be.
*E-mail: Pascal.VanDerVoort@UGent.be.
*E-mail: Kurt.Lejaeghere@UGent.be.

ORCID

Jonas J. Joos: 0000-0002-7869-2217
Arthur De Vos: 0000-0002-4916-6066
Philippe F. Smet: 0000-0003-4789-5799
Veronique Van Speybroeck: 0000-0003-2206-178X
Pascal Van Der Voort: 0000-0002-4874-0943
Kurt Lejaeghere: 0000-0002-4462-8209

Notes

The authors declare no competing financial interest.

■ ACKNOWLEDGMENTS

The Fund for Scientific Research-Flanders (FWO) and the Research Board of Ghent University (BOF) are acknowledged for their financial support. Computational resources and services were provided by the Stevin Supercomputer Infrastructure of Ghent University and by the Flemish Supercomputer Center (VSC), funded by the Hercules Foundation and the Flemish Government - Department EWI.

■ REFERENCES

(1) Thematic Issue: Metal−Organic Frameworks. *Chem. Rev.* **2012**, *112*, 673−1268.

(2) Zhou, H.; Kitagawa, S. Metal-Organic Frameworks (MOFs). *Chem. Soc. Rev.* **2014**, *43*, 5415−5418.

(3) Maurin, G.; Serre, C.; Cooper, A.; Férey, G. The new age of MOFs and of their porous-related solids. *Chem. Soc. Rev.* **2017**, *46*, 3104−3107.

(4) Santaclara, J.; Kapteijn, F.; Gascon, J.; van der Veen, M. Understanding metal-organic frameworks for photocatalytic solar fuel production. *CrystEngComm* **2017**, *19*, 4118−4125.

(5) Allendorf, M. D.; Bauer, C. A.; Bhakta, R. K.; Houk, R. J. T. Luminescent metal-organic frameworks. *Chem. Soc. Rev.* **2009**, *38*, 1330−1352.

(6) Wang, J.; Wang, C.; Lin, W. Metal-Organic Frameworks for Light Harvesting and Photocatalysis. *ACS Catal.* **2012**, *2*, 2630−2640.

(7) Nasalevich, M. A.; van der Veen, M.; Kapteijn, F.; Gascon, J. Metal-organic frameworks as heterogeneous photocatalysts: advantages and challenges. *CrystEngComm* **2014**, *16*, 4919−4926.

(8) Lustig, W. P.; Mukherjee, S.; Rudd, N. D.; Desai, A. V.; Li, J.; Ghosh, S. K. Metal-organic frameworks: functional luminescent and photonic materials for sensing applications. *Chem. Soc. Rev.* **2017**, *46*, 3242−3285.

(9) De Vos, A.; Hendrickx, K.; Van Der Voort, P.; Van Speybroeck, V.; Lejaeghere, K. Missing linkers: an alternative pathway to UiO-66 electronic structure engineering. *Chem. Mater.* **2017**, *29*, 3006−3019.

(10) Yu, Y.; Chen, G.; Zhou, Y.; Han, Z. Recent advances in rare-earth elements modification of inorganic semiconductor-based photocatalysts for efficient solar energy conversion: A review. *J. Rare Earths* **2015**, *33*, 453−462.

(11) Kumar, G. S.; Devi, G. L. Review on Modified TiO_2 Photocatalysis under UV/Visible Light: Selected Results and Related Mechanisms on Interfacial Charge Carrier Transfer Dynamics. *J. Phys. Chem. A* **2011**, *115*, 13211−13241.

(12) Qin, X.; Liu, X.; Huang, W.; Bettinelli, M.; Liu, X. Lanthanide-Activated Phosphors Based on 4f-5d Optical Transitions: Theoretical and Experimental Aspects. *Chem. Rev.* **2017**, *117*, 4488−4527.

(13) Cheng, P. *Lanthanide Metal−Organic Frameworks*; Structure and Bonding series; Springer: Berlin, 2014.

(14) Xu, H.; Cao, C.; Kang, X.; Zhao, B. Lanthanide-based metal-organic frameworks as luminescent probes. *Dalton Trans.* **2016**, *45*, 18003−18017.

(15) Pagis, C.; Ferbinteanu, M.; Rothenberg, G.; Tanase, S. Lanthanide-Based Metal-Organic Frameworks: Synthetic Strategies and Catalytic Applications. *ACS Catal.* **2016**, *6*, 6063−6072.

(16) Liang, Y.; Yang, G.; Liu, B.; Yan, Y.; Xi, Z.; Wang, Y. Four super water-stable lanthanide-organic frameworks with active uncoordinated carboxylic and pyridyl groups for selective luminescence sensing of Fe^{3+}. *Dalton Trans.* **2015**, *44*, 13325−13330.

(17) Tu, J.; Zeng, X.; Xu, F.; Wu, X.; Tian, Y.; Hou, X.; Long, Z. Microwave-induced fast incorporation of titanium into UiO-66 metal-organic frameworks for enhanced photocatalytic properties. *Chem. Commun.* **2017**, *53*, 3361−3364.

(18) Leus, K.; Bogaerts, T.; De Decker, J.; Depauw, H.; Hendrickx, K.; Vrielinck, H.; Van Speybroeck, V.; Van Der Voort, P. Systematic study of the chemical and hydrothermal stability of selected "stable" Metal Organic Frameworks. *Microporous Mesoporous Mater.* **2016**, *226*, 110−116.

(19) Cavka, J. H.; Jakobsen, S.; Olsbye, U.; Guillou, N.; Lamberti, C.; Bordiga, S.; Lillerud, K. P. A new zirconium inorganic building brick forming metal organic frameworks with exceptional stability. *J. Am. Chem. Soc.* **2008**, *130*, 13850−13851.

(20) Valenzano, L.; Civalleri, B.; Chavan, S.; Bordiga, S.; Nilsen, M. H.; Jakobsen, S.; Lillerud, K. P.; Lamberti, C. Disclosing the Complex

Structure of UiO-66 Metal Organic Framework: A Synergic Combination of Experiment and Theory. *Chem. Mater.* **2011**, *23*, 1700−1718.

(21) Marshall, R. J.; Forgan, R. S. Postsynthetic Modification of Zirconium Metal-Organic Frameworks. *Eur. J. Inorg. Chem.* **2016**, *2016*, 4310−4331.

(22) Kim, M.; Cahill, J. F.; Fei, H.; Prather, K. A.; Cohen, S. M. Postsynthetic Ligand and Cation Exchange in Robust Metal-Organic Frameworks. *J. Am. Chem. Soc.* **2012**, *134*, 18082−18088.

(23) Smith, S. J.; Ladewig, B. P.; Hill, A. J.; Lau, C.; Hill, M. R. Post-synthetic Ti Exchanged UiO-66 Metal-Organic Frameworks that Deliver Exceptional Gas Permeability in Mixed Matrix Membranes. *Sci. Rep.* **2015**, *5*, 7823.

(24) Sun, D.; Liu, W.; Qiu, M.; Zhang, Y.; Li, Z. Introduction of a mediator for enhancing photocatalytic performance via post-synthetic metal exchange in metal-organic frameworks (MOFs). *Chem. Commun.* **2015**, *51*, 2056−2059.

(25) Lee, Y.; Kim, S.; Kang, J.; Cohen, S. M. Photocatalytic CO_2 reduction by a mixed metal (Zr/Ti), mixed ligand metal-organic framework under visible light irradiation. *Chem. Commun.* **2015**, *51*, 5735−5738.

(26) Wang, A.; Zhou, Y.; Wang, Z.; Chen, M.; Sun, L.; Liu, X. Titanium incorporated with UiO-66(Zr)-type Metal-Organic Framework (MOF) for photocatalytic application. *RSC Adv.* **2016**, *6*, 3671−3679.

(27) Nasalevich, M. A.; Hendon, C. H.; Santaclara, J. G.; Svane, K.; van der Linden, B.; Veber, S. L.; Fedin, M. V.; Houtepen, A. J.; van der Veen, M. A.; Kapteijn, F.; Walsh, A.; Gascon, J. Electronic origins of photocatalytic activity in d^0 metal organic frameworks. *Sci. Rep.* **2016**, *6*, 23676.

(28) Yasin, A.; Li, J.; Wu, N.; Musho, T. Study of the inorganic substitution in a functionalized UiO-66 metal-organic framework. *Phys. Chem. Chem. Phys.* **2016**, *18*, 12748−12754.

(29) Yang, L.; Ganz, E.; Svelle, S.; Tilset, M. Computational exploration of newly synthesized zirconium metal-organic frameworks UiO-66, −67, −68 and analogues. *J. Mater. Chem. C* **2014**, *2*, 7111−7125.

(30) Santiago-Portillo, A.; Baldovi, H.; García Fernandez, M. T.; Navalon, S.; Atienzar, P.; Ferrer, B.; Alvaro, M.; Garcia, H.; Li, Z. Ti as Mediator in the Photoinduced Electron Transfer of Mixed-Metal NH_2-UiO66(Zr/Ti). Transient Absorption Spectroscopy Study and Application in Photovoltaic Cell. *J. Phys. Chem. C* **2017**, *121*, 7015−7024.

(31) Dorenbos, P. A Review on How Lanthanide Impurity Levels Change with Chemistry and Structure of Inorganic Compounds. *ECS J. Solid State Sci. Technol.* **2013**, *2*, R3001−R3011.

(32) Joos, J. J.; Poelman, D.; Smet, P. F. Energy level modeling of lanthanide materials: review and uncertainty analysis. *Phys. Chem. Chem. Phys.* **2015**, *17*, 19058−19078.

(33) Seijo, L.; Barandiarán, Z. Ab Initio Calculations on Excited States of Lanthanide Containing Materials; In *Handbook on the Physics and Chemistry of Rare Earths*; Gschneidner, K. A., Eyring, L., Eds.; Elsevier: New York, 2016.

(34) Biswas, S.; Van Der Voort, P. A General Strategy for the Synthesis of Functionalised UiO-66 Frameworks: Characterisation, Stability and CO_2 Adsorption Properties. *Eur. J. Inorg. Chem.* **2013**, *2013*, 2154−2160.

(35) Lammert, M.; Wharmby, M. T.; Smolders, S.; Bueken, B.; Lieb, A.; Lomachenko, K. A.; De Vos, D.; Stock, N. Cerium-based metal organic frameworks with UiO-66 architecture: synthesis, properties and redox catalytic activity. *Chem. Commun.* **2015**, *51*, 12578−12581.

(36) Görller-Walrand, C.; Binnemans, K. Rationalization of crystal-field parametrization. In *Handbook on the Physics and Chemistry of Rare Earths*; Gschneidner, K. A., Eyring, L., Eds.; Elsevier: New York, 1996.

(37) Rogers, E.; Dorenbos, P. Vacuum energy referred $Ti^{3+/4+}$ donor/acceptor states in insulating and semiconducting inorganic compounds. *J. Lumin.* **2014**, *153*, 40−45.

(38) Levin, J. R.; Dorfner, W. L.; Dai, A. X.; Carroll, P. J.; Schelter, E. J. Density Functional Theory as a Predictive Tool for Cerium Redox Properties in Nonaqueous Solvents. *Inorg. Chem.* **2016**, *55*, 12651−12659.

(39) Loschen, C.; Migani, A.; Bromley, S. T.; Illas, F.; Neyman, K. M. Density functional studies of model cerium oxide nanoparticles. *Phys. Chem. Chem. Phys.* **2008**, *10*, 5730−5738.

(40) Frisch, M. J.; Trucks, G. W.; Schlegel, H. B.; Scuseria, G. E.; Robb, M. A.; Cheeseman, J. R.; Scalmani, G.; Barone, V.; Mennucci, B.; Petersson, G. A.; Nakatsuji, H.; Caricato, M.; Li, X.; Hratchian, H. P.; Izmaylov, A. F.; Bloino, J.; Zheng, G.; Sonnenberg, J. L.; Hada, M.; Ehara, M.; Toyota, K.; Fukuda, R.; Hasegawa, J.; Ishida, M.; Nakajima, T.; Honda, Y.; Kitao, O.; Nakai, H.; Vreven, T.; Montgomery, J. A., Jr.; Peralta, J. E.; Ogliaro, F.; Bearpark, M.; Heyd, J. J.; Brothers, E.; Kudin, K. N.; Staroverov, V. N.; Kobayashi, R.; Normand, J.; Raghavachari, K.; Rendell, A.; Burant, J. C.; Iyengar, S. S.; Tomasi, J.; Cossi, M.; Rega, N.; Millam, J. M.; Klene, M.; Knox, J. E.; Cross, J. B.; Bakken, V.; Adamo, C.; Jaramillo, J.; Gomperts, R.; Stratmann, R. E.; Yazyev, O.; Austin, A. J.; Cammi, R.; Pomelli, C.; Ochterski, J. W.; Martin, R. L.; Morokuma, K.; Zakrzewski, V. G.; Voth, G. A.; Salvador, P.; Dannenberg, J. J.; Dapprich, S.; Daniels, A. D.; Farkas, O.; Foresman, J. B.; Ortiz, J. V.; Cioslowski, J.; Fox, D. J. *Gaussian 09*, revision D.01; Gaussian, Inc.: Wallingford, CT, 2009.

(41) Hendrickx, K.; Vanpoucke, D. E. P.; Leus, K.; Lejaeghere, K.; Van Yperen-De Deyne, A.; Van Speybroeck, V.; Van Der Voort, P.; Hemelsoet, K. Understanding Intrinsic Light Absorption Properties of UiO-66 Frameworks: A Combined Theoretical and Experimental Study. *Inorg. Chem.* **2015**, *54*, 10701−10710.

(42) Lee, C.; Yang, W.; Parr, R. G. Development of the Colle-Salvetti correlation-energy formula into a functional of the electron density. *Phys. Rev. B: Condens. Matter Mater. Phys.* **1988**, *37*, 785−789.

(43) Becke, A. D. Density-functional thermochemistry. III. The role of exact exchange. *J. Chem. Phys.* **1993**, *98*, 5648−5652.

(44) Weigend, F.; Ahlrichs, R. Balanced basis sets of split valence, triple zeta valence and quadruple zeta valence quality for H to Rn: Design and assessment of accuracy. *Phys. Chem. Chem. Phys.* **2005**, *7*, 3297−3305.

(45) Freysoldt, C.; Grabowski, B.; Hickel, T.; Neugebauer, J.; Kresse, G.; Janotti, A.; Van de Walle, C. G. First-principles calculations for point defects in solids. *Rev. Mod. Phys.* **2014**, *86*, 253−305.

(46) Runge, E.; Gross, E. K. U. Density-functional theory for time-dependent systems. *Phys. Rev. Lett.* **1984**, *52*, 997−1001.

(47) Marques, M. A. L., Ullrich, C., Nogueira, F., Rubio, A., Burke, K., Gross, E. K. U., Eds. *Time-Dependent Density Functional Theory*; Lecture Notes in Physics; Springer-Verlag: Berlin, 2006.

(48) Dreuw, A.; Head-Gordon, M. Single-Reference ab Initio Methods for the Calculation of Excited States of Large Molecules. *Chem. Rev.* **2005**, *105*, 4009−4037.

(49) Kresse, G.; Furthmüller, J. Efficiency of ab-initio total energy calculations for metals and semiconductors using a plane-wave basis set. *Comput. Mater. Sci.* **1996**, *6*, 15−50.

(50) Hafner, J. Ab-Initio Simulations of Materials Using VASP: Density-Functional Theory and Beyond. *J. Comput. Chem.* **2008**, *29*, 2044−2078.

(51) Kresse, G.; Joubert, D. From ultrasoft pseudopotentials to the projector augmented-wave method. *Phys. Rev. B: Condens. Matter Mater. Phys.* **1999**, *59*, 1758−1775.

(52) Lejaeghere, K.; et al. Reproducibility in density functional theory calculations of solids. *Science* **2016**, *351*, aad3000.

(53) Perdew, J. P.; Burke, K.; Ernzerhof, M. Generalized Gradient Approximation Made Simple. *Phys. Rev. Lett.* **1996**, *77*, 3865−3868.

(54) Vinet, P.; Ferrante, J.; Rose, J.; Smith, J. Compressibility of solids. *J. Geophys. Res.* **1987**, *92*, 9319.

(55) Brozek, C. K.; Dincă, M. Cation exchange at the secondary building units of metal-organic frameworks. *Chem. Soc. Rev.* **2014**, *43*, 5456−5467.

(56) Zhao, J.; Mi, L.; Hu, J.; Hou, H.; Fan, Y. Cation Exchange Induced Tunable Properties of a Nanoporous Octanuclear Cu(II) Wheel with Double-Helical Structure. *J. Am. Chem. Soc.* **2008**, *130*, 15222−15223.

(57) Son, D.; Hughes, S. M.; Yin, Y.; Alivisatos, P. A. Cation Exchange Reactions in Ionic Nanocrystals. *Science* **2004**, *306*, 1009−1012.

(58) Fei, H.; Pham, C. H.; Oliver, S. R. J. Anion Exchange of the Cationic Layered Material $[Pb_2F_2]^{2+}$. *J. Am. Chem. Soc.* **2012**, *134*, 10729−10732.

(59) Wißmann, G.; Schaate, A.; Lilienthal, S.; Bremer, I.; Schneider, A. M.; Behrens, P. Modulated synthesis of Zr-fumarate MOF. *Microporous Mesoporous Mater.* **2012**, *152*, 64−70.

(60) Santaclara, J. G.; Olivos-Suarez, A. I.; Gonzalez-Nelson, A.; Osadchii, D.; Nasalevich, M. A.; van der Veen, M. A.; Kapteijn, F.; Sheveleva, A. M.; Veber, S. L.; Fedin, M. V.; Murray, A. T.; Hendon, C. H.; Walsh, A.; Gascon, J. Revisiting the Incorporation of Ti(IV) in UiO-type Metal-Organic Frameworks: Metal Exchange versus Grafting and Their Implications on Photocatalysis. *Chem. Mater.* **2017**, *29*, 8963−8967.

(61) Janulevicius, M.; Marmokas, P.; Misevicius, M.; Grigorjevaite, J.; Mikoliunaite, L.; Sakirzanovas, S.; Katelnikovas, A. Luminescence and luminescence quenching of highly efficient $Y_2Mo_4O_{15}$:Eu^{3+} phosphors and ceramics. *Sci. Rep.* **2016**, *6*, 26098.

(62) Liu, Y.; Decadt, R.; Bogaerts, T.; Hemelsoet, K.; Kaczmarek, A. M.; Poelman, D.; Waroquier, M.; Van Speybroeck, V.; Van Deun, R.; Van Der Voort, P. Bipyridine-Based Nanosized Metal-Organic Framework with Tunable Luminescence by a Postmodification with Eu(III): An Experimental and Theoretical Study. *J. Phys. Chem. C* **2013**, *117*, 11302−11310.

(63) Dorenbos, P. Ce^{3+} 5d-centroid shift and vacuum referred 4f-electron binding energies of all lanthanide impurities in 150 different compounds. *J. Lumin.* **2013**, *135*, 93−104.

(64) Hoefdraad, H. Charge-transfer spectra of tetravalent lanthanide ions in oxides. *J. Inorg. Nucl. Chem.* **1975**, *37*, 1917−1921.

(65) Seijo, L.; Barandiarán, Z. Intervalence charge transfer luminescence: The anomalous luminescence of cerium-doped $Cs_2LiLuCl_6$ elpasolite. *J. Chem. Phys.* **2014**, *141*, 214706.

(66) Heyd, J.; Scuseria, G. E.; Ernzerhof, M. Hybrid functionals based on a screened Coulomb potential. *J. Chem. Phys.* **2003**, *118*, 8207−8215.

(67) Heyd, J.; Scuseria, G. E.; Ernzerhof, M. J. Erratum: Hybrid functionals based on a screened Coulomb potential [J. Chem. Phys.118, 8207 (2003)]. *J. Chem. Phys.* **2006**, *124*, 219906.

(68) Chakrabarty, A.; Patterson, C. H. Transition levels of defects in ZnO: Total energy and Janak's theorem methods. *J. Chem. Phys.* **2012**, *137*, 054709.

(69) Broqvist, P.; Alkauskas, A.; Pasquarello, A. Hybrid-functional calculations with plane-wave basis sets: Effect of singularity correction on total energies, energy eigenvalues, and defect energy levels. *Phys. Rev. B: Condens. Matter Mater. Phys.* **2009**, *80*, 085114.

(70) Gallino, F.; Pacchioni, G.; Di Valentin, C. D. Transition levels of defect centers in ZnO by hybrid functionals and localized basis set approach. *J. Chem. Phys.* **2010**, *133*, 144512.

(71) Joos, J. J.; Lejaeghere, K.; Korthout, K.; Feng, A.; Poelman, D.; Smet, P. F. Charge transfer induced energy storage in CaZnOS:Mn - insight from experimental and computational spectroscopy. *Phys. Chem. Chem. Phys.* **2017**, *19*, 9075−9085.